J Solid State Electrochem (2012) 16:2179–2186
DOI 10.1007/s10008-012-1639-1

ORIGINAL PAPER

Preparation of activated carbon from waste *Camellia oleifera* shell for supercapacitor application

Juntao Zhang · Liangyu Gong · Kang Sun · Jianchun Jiang · Xiaogang Zhang

Received: 29 August 2011 / Revised: 22 December 2011 / Accepted: 2 January 2012 / Published online: 17 January 2012

Abstract The cost-effective activated carbons derived from waste *Camellia oleifera* shell (COS) by $ZnCl_2$ activation method are investigated as the active electrode material in electric double-layer capacitors (EDLCs) for the first time. The activation temperature and $ZnCl_2$/COS impregnation ratio are two key factors affecting the surface area and pore structure of the prepared activated carbons, which accordingly affect their capacitive performances. Electrochemical investigations indicate that the activated carbon (AC-3-600) obtained at the activation temperature of 600 °C and impregnation ratio of 3 shows the maximum specific capacitance of 374 and 266 $F g^{-1}$ in 1 mol L^{-1} H_2SO_4 and 6 mol L^{-1} KOH electrolytes at 0.2 A g^{-1}, respectively. The high capacitance of the AC-3-600 is attributed to its high surface area (1,935 m^2 g^{-1}), high total pore volume (1.02 cm^3 g^{-1}), and especially the large percentage of micropores (735 m^2 g^{-1}). Meanwhile, the activated carbon presents good cycle stability in both acid and alkaline electrolytes during 5,000 cycles at a fair current density of 4 A g^{-1}. So, we had reasons to believe that the activated carbons from waste COS by $ZnCl_2$ activation might be one of the innovative carbon electrode materials for EDLCs application.

Keywords *Camellia oleifera* shell · $ZnCl_2$ activation · Carbon electrodes · Electrochemical properties

Introduction

Electric double-layer capacitors (EDLCs) have recently become one of the hottest research topics due to their potential in high power output and high energy density applications [1–3]. Therefore, tremendous efforts have been devoted to developing active electrode materials for EDLCs applications. Various carbon-based materials such as activated carbon (AC) [4], carbon nanotubes [5, 6], carbon aerogel [7], graphene [8, 9], and graphene-based composites [10] are currently investigated as active electrode materials for EDLCs. Among them, activated carbon enjoys a place of pride as a consequence of its abundance, cost-effectiveness, and environmentally benign nature [11]. Recently, the utilization of biomass materials, especially agricultural and industrial by-products, such as sunflower seed shells [12], banana fibers [11], coffee grounds [13], corn grains [14], fir wood [15], needle cokes [16], bombyx mori silk fibroins [17], seaweeds [18], bagasse [19], etc., as precursors to prepare activated carbons for EDLCs applications has attracted much attention due to the high cost of commercial activated carbon produced from coal.

Camellia oleifera is an important woody oil crop in China with a planting area of about 3.5×10^6 hm^2 and annual yield of about 560 million tonnes [20]. Plenty of COS was produced as biowaste from *C. oleifera* processing every year and it is mostly burned for the purpose of quick disposal,

Electronic supplementary material The online version of this article (doi:10.1007/s10008-012-1639-1) contains supplementary material, which is available to authorized users.

J. Zhang · L. Gong (✉)
College of Chemistry and Pharmaceutical Sciences,
Qingdao Agricultural University,
Qingdao 266109, People's Republic of China
e-mail: lygong@163.com

X. Zhang (✉)
College of Material Science and Engineering,
Nanjing University of Aeronautics and Astronautics,
Nanjing 210016, People's Republic of China
e-mail: azhangxg@163.com

K. Sun · J. Jiang
Institute of Chemical Industry of Forest Products,
Nanjing 210042, People's Republic of China

which indicates that this biowaste is a cheap raw material resource for the preparation of activated carbon. Herein, we report EDLCs performance of carbon materials derived from COS for the first time. The effects of process conditions, including the activation temperature and $ZnCl_2$/COS impregnation ratio, on the surface area, pore structure, and subsequently electrochemical performance of the activated carbons have also been discussed in detail.

Experimental

Materials and methods

The precursor used for the preparation of the activated carbons was COS (Hunan, China). It was washed thoroughly with distilled water to remove soil and clay and then dried at 100 °C in an oven for 24 h. In a typical synthesis experiment, the dried COS was refluxed in 2 mol L^{-1} NaOH solution at 100 °C for 12 h. After consequent centrifuging, rinsing with copious distilled water, and drying, the treated COS was impregnated with $ZnCl_2$ solutions at $ZnCl_2$/COS impregnation ratios of 2, 3, and 4, respectively. The impregnated samples were put into a 110 °C oil bath to remove excess water, then oven-dried at 110 °C for 12 h, and finally carbonized in a tube furnace at various temperatures of 500, 600, and 700 °C for 1 h under N_2 flow, respectively. The carbonized samples were washed with 0.5 mol L^{-1} HCl and hot distilled water repeatedly for the removal of excess zinc chloride and then dried at 110 °C for 24 h. The resultant activated carbons were labeled as AC-*x*-*y*, where *x* represents the impregnation ratio and *y* represents the carbonization temperature.

Structure and texture characterization

The N_2 adsorption–desorption isotherms of the resulting activated carbons were recorded under −196 °C on ASAP 2010 analyzer (Micromeritics, USA). Brunauer–Emmett–Teller (BET) surface area was calculated by using the BET equation. Total pore volume was obtained at p/p^0=0.995. Micropore surface area and micropore volume were calculated by t-plot method. Elemental analyses for the activated carbons (ACs) were performed on Heraeus CHN-O rapid elemental analyzer (Germany). Thermal gravimetric analysis (TGA) was carried out with a thermal analyzer (Netzsch STA 409 PC, Germany) at a heating rate of 5 °C min^{-1} under N_2 atmosphere. The morphology of the synthesized samples was examined by using transmission electron microscope (TEM) and scanning electron microscope (SEM) images, which were taken on FEI Tencnai G^2 20S-TWIN microscope equipped with energy dispersive X-ray spectrometer (EDAX Gensis) and LEO1430VP microscope, respectively.

Electrochemical measurements

Electrochemical measurements were carried out in a three-electrode single-cell system using platinum plate and saturated calomel electrode (SCE) as counter electrode and reference electrode, respectively. The working electrodes were fabricated by mixing the resulting activated carbons with 5% acetylene black and 5% polytetrafluoroethylene. The slurry was further painted onto the graphite groove (area, 1 cm^2) and dried. The cyclic voltammetry (CV) and galvanostatic charge–discharge measurements were performed on a CHI660C electrochemical analyzer system (Chenhua, Shanghai, China) and the cyclic charge–discharge tests were evaluated with a Land CT2001A battery program–control test system (LAND, Wuhan, China) in 6 mol L^{-1} KOH and 1 mol L^{-1} H_2SO_4 electrolytes at room temperature, respectively.

Results and discussion

Thermal gravimetric analysis

The thermal behaviors of the COS and the impregnated COS with $ZnCl_2$ at impregnation ratios of 2, 3, and 4 have been investigated by TGA. As presented in Fig. 1, a small amount of weight loss occurs at around 30–150 °C in all the TGA curves owing to water evaporation. Then, the TGA curves were distinctly different between the COS and impregnated COS. As the temperature increases to 150–450 °C, a significant weight loss of about 70% for COS appears, which is attributed to the dehydration and release of volatiles from the cellulosic structure. However, the impregnated COS undergo much lower weight loss (about 10%) at the same

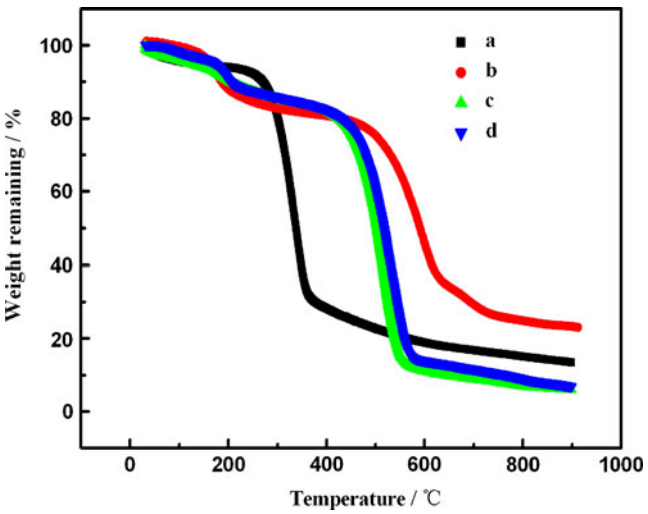

Fig. 1 Thermal gravimetric analyses of COS (**a**) and impregnated COS with $ZnCl_2$ at impregnation ratios of 2 (**b**), 3 (**c**), and 4 (**d**) in N_2

temperature range, which is associated with the dehydration of the carbon precursor and the volatilization of cellulosic fractions of the COS. The substantially lower loss of weight than that suffered by the untreated COS suggests that the consequential decrease in the evolution of volatiles would result in higher activated carbon yield from COS [19], which can be further proved by elemental analysis of activated carbons from the untreated COS and the impregnated COS with $ZnCl_2$ at impregnation ratios of 3. As shown in Table 1, the content of carbon in AC-3-600 is much higher than in the activated carbons (AC-0-600) from untreated COS. The significant weight loss of about 60–75% for impregnated COS occurs between 450 and 700 °C, which should be attributed to the volatilization of $ZnCl_2$ and the carbon mass loss via active pyrolysis and aromatic condensation reactions [19]. Figure 1 also shows the discrepancies in thermal behavior of the impregnated COS samples. The impregnated COS at impregnation ratios of 3 and 4 produce a higher mass loss and instantaneous rate of thermal decomposition. At the same time, they have a lower temperature and shorter duration for COS pyrolysis, suggesting that the activation reactions at impregnation ratios of 3 and 4 occur faster and more easily than that at the impregnation ratio of 2.

Pore texture of activated carbons

Figure 2 shows nitrogen adsorption–desorption isotherms of ACs derived from COS by chemical activation with $ZnCl_2$ at various impregnation ratios and activation temperatures. It can be seen that the isotherms of the ACs are of different types. The isotherms of AC-2-*y* and AC-3-*y* exhibit type I characteristics, indicating the samples mainly comprise micropores and small parts of mesopores. As for AC-4-600 obtained with a higher impregnation ratio of 4, a small hysteresis loop at the high relative pressure region (p/p^0> 0.5) can be observed, demonstrating the existence of mesopores with larger pore size.

The surface area and pore structure parameters of the activated carbons are summarized in Table 2. As shown in Table 2, the BET surface area (S_{BET}) and total pore volume increase as the activation temperature changing from 500 to 600 °C but decrease when the activation temperature is higher than 600 °C. The activation temperature of 600 °C

Table 1 Results of elemental analysis of the activated carbons (AC-0-600 and AC-3-600) from COS and impregnated COS with $ZnCl_2$ at impregnation ratios of 3, respectively

ACs	Elemental composition (wt.%)		
	Carbon	Hydrogen	Nitrogen
AC-0-600	72.31	4.34	–
AC-3-600	89.44	2.23	0.32

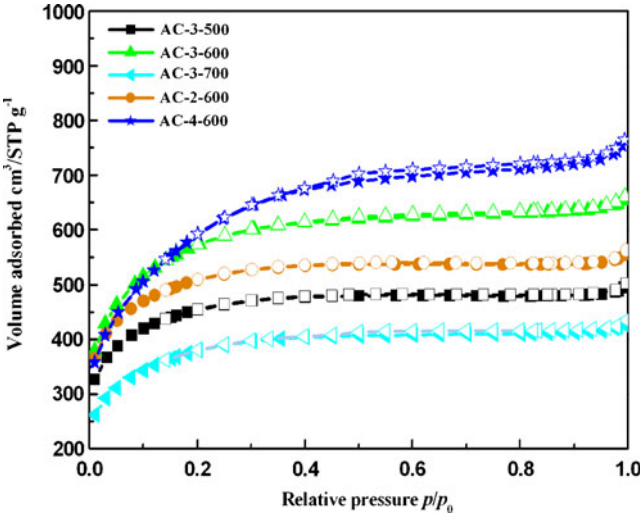

Fig. 2 Nitrogen adsorption/desorption isotherms (*closed*/*open symbols*) at −196 °C for activated carbons obtained from COS with different impregnation ratios

is demonstrated to be effective to generate pore structure for activated carbons. A possible explanation is as follows: the activation reactions occur faster at 600 °C than at 500 °C, resulting in more channels accordingly. The reduction in both surface area and pore volume as activation temperature increasing to 700 °C results from $ZnCl_2$ volatilization and pore shrinkage effect [19]. When the activation temperature is kept unchanged at 600 °C and only the impregnation ratios are adjusted, the BET area increases from 1,687 to 2,080 $m^2\ g^{-1}$ and the total pore volume rises from 0.87 to 1.18 $cm^3\ g^{-1}$ with increase in the impregnation ratios from 2 to 4, and mesopore surface area and mesopore volume follow the same trend. Among the samples, AC-4-600 possesses the highest BET surface area (2,080 $m^2\ g^{-1}$) and total pore volume (1.18 $cm^3\ g^{-1}$). It is worthwhile to mention that the micropore surface area and volume decreased with increasing impregnation ratios, which may be attributed to the micropore collapse caused by over-activation. The breakage that occurred in the walls between the adjacent micropores may result in the formation of mesopores [21], which may also explain the phenomenon of the mesopore surface area of AC-4-600 being higher than that of AC-3-600.

SEM and TEM examinations of COS and prepared activated carbon

Figure 3 depicts the SEM images of carbon precursor and the resulting activated carbon (AC-3-600). As shown in Fig. 3a, the carbon precursor presents large thin sheets and there are many folds on the surface. Figure 3b, a higher-magnification image of this sample, indicates that there are a lot of homogeneous small holes on the surface of the carbon precursor, which promote the impregnation of carbon precursor with

Table 2 Surface texture properties of activated carbons derived from COS

Carbonization temperature (°C)	S_{BET} ($m^2\ g^{-1}$)	S_{mi}[a] ($m^2\ g^{-1}$)	S_{me}[b] ($m^2\ g^{-1}$)	V_{tot}[c] ($cm^3\ g^{-1}$)	V_{mi}[d] ($cm^3\ g^{-1}$)	V_{me}[e] ($cm^3\ g^{-1}$)	$Pore_{av}$[f] diameter (nm)
AC-3-500	1,508	764	743	0.78	0.38	0.40	2.1
AC-3-600	1,935	735	1,200	1.02	0.32	0.7	2.1
AC-3-700	1,270	565	713	0.67	0.27	0.40	2.1
AC-2-600	1,687	875	812	0.87	0.44	0.43	2.0
AC-4-600	2,080	265	1,815	1.18	0.12	1.06	2.3

[a] Micropore surface area derived from t-plot method

[b] Mesopore surface area calculated by subtraction of micropore surface area from BET surface area

[c] Total pore volume measured at $p/p^0 = 0.995$

[d] Micropore pore volume derived from t-plot method

[e] Mesopore volume calculated by subtraction of micropore volume from total pore volume

[f] Average pore diameter of porous carbon calculated by $4V_T/S_{BET}$

$ZnCl_2$, thereby facilitating the fabrication of high-surface-area activated carbon. After the process of high temperature activation, carbon precursor sheet falls apart and activated carbon block appears (Fig. 3c) due to the decomposition of cellulosic materials and the release of volatiles. Figure 3d further vividly illustrates the pore structure evolvement of the porous carbons after activation. Compared with carbon precursor, it is found that the holes with different size replace the homogeneous small holes on the surface of the carbon precursor. Meanwhile, a large number of wormhole-like micropores are also found in the TEM images (Fig. 3e, f) after activation.

Electrochemical measurements

The capacitive behaviors of the as-prepared samples were estimated by CV and galvanostatic charge–discharge measurements and the results are shown in Fig. 4. As shown in Fig. 4a, the shape of the CV curves for all ACs at a scan rate of 5 mV s^{-1} within the potential range of −0.2–0.8 V (vs. SCE) in 1 mol L^{-1} H_2SO_4 electrolyte was more or less (quasi-) rectangular. In addition, some redox peaks are also clearly observed, which is usually attributed to pseudo-Faradic reactions involving the oxygenated functional groups presenting in the surface of activated carbon. Therefore, the specific capacitances of the ACs are composed of electric double-layer capacitances and pseudo-capacitances. The CV curve of AC-3-600 exhibits the biggest current response and covers the largest area, suggesting that AC-3-600 has the highest specific capacitance. Figure 4b compares the charge/discharge curves of all the ACs recorded in 1 mol L^{-1} H_2SO_4 electrolyte at the current density of 1 A g^{-1} between −0.2 and 0.8 V (vs. SCE) at the first cycle. Obviously, all the charge/discharge profiles exhibit almost the isosceles triangle curves, demonstrating the simulative capacitors with the performance of electrochemical stability and reversibility. The specific capacitance of AC-3-600, AC-4-600, and AC-2-600 are 282, 270, and 260 $F\,g^{-1}$ at 1 A g^{-1}, respectively. There has been a little decrease in the specific capacitance when the activation temperature is lower or higher than 600 °C. For example, AC-3-500 and AC-3-700 can only deliver a slightly lower capacitance of 227 and 215 $F\,g^{-1}$, respectively. This result indicates the dependence of specific capacitance on the activation temperature. It can be understood that the excellent capacitive performance of AC-*x*-600 is attributed to their high specific surface area as shown in Table 2. The capacitive disparities among AC-3-600, AC-4-600, and AC-2-600 samples further show the relationship between specific capacitance and impregnation ratio. By contrast, AC-2-600 indicates the lowest specific capacitance among the three samples which may be due to its lowest surface area. It is worth noting that the specific capacitance of AC-3-600 is higher than that of AC-4-600 although the later possesses a larger specific surface area. This is mainly ascribed to the larger percentage of micropores (735 $m^2\ g^{-1}$) in the texture of AC-3-600, which contributes more to EDLCs than mesopores [12]. Figure 4c depicts the dependence of specific capacitance on the current density. The specific capacitance of AC-600-3 is much higher than that of the others at all current densities and it presents the highest specific capacitance of 374 $F\,g^{-1}$ at the current density of 0.2 A g^{-1}, which is in agreement with the result of the CVs in Fig. 4a. The capacitance decreases slightly with the increase of current density and it drops to 190 $F\,g^{-1}$ at the current density of 10 A g^{-1}, remaining 50.8% of that measured at 0.2 A g^{-1}. As for AC-4-600, it has a specific capacitance of 353 $F\,g^{-1}$ at the current density of 0.2 A g^{-1} and 177 $F\,g^{-1}$ at the current density of 10 A g^{-1}, remaining 50.2% of the former.

Figure 5a depicts the detailed CV behaviors of AC-3-600 at scan rates of 2, 5, 10, 20, 50, and 100 mV s^{-1} in 1 mol L^{-1} H_2SO_4 electrolyte. As shown in Fig. 5a, when the scan rate ranges from 5 to 50 mV s^{-1}, the quasi-rectangular shape can still remain, indicating excellent capacitive behavior. However, the serious distortion of

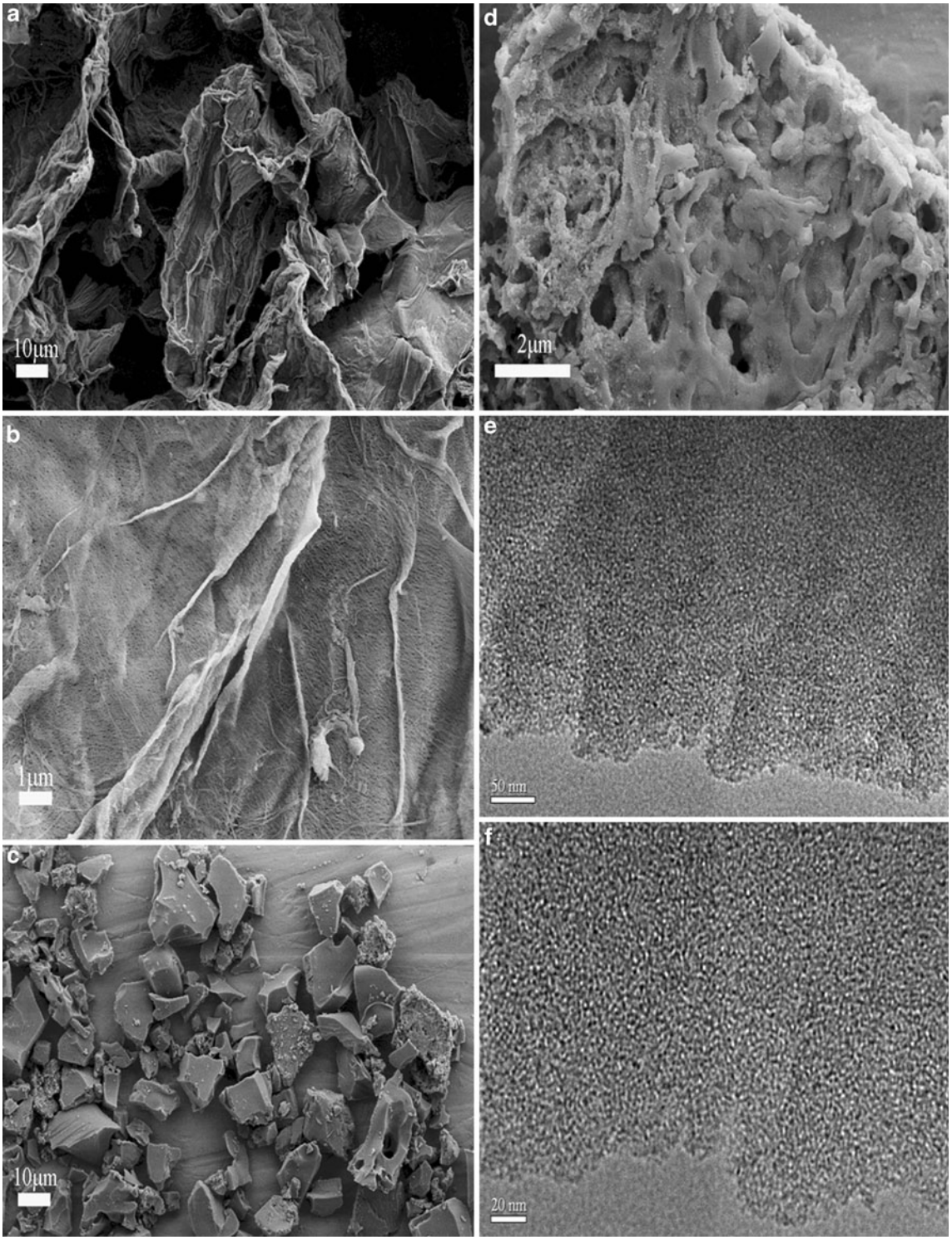

Fig. 3 The SEM images of carbon precursor (**a**, **b**) and the SEM (**c**, **d**) and TEM (**e**, **f**) images of the activated carbons Ac-3-600

CV profiles is presented at a high scan rate of 100 mV s^{-1}, and similar results have also been observed for other activated carbons when the scan rate is higher than 50 mV s^{-1} [11, 22]. The CV behaviors of AC-3-600 in 6 mol L^{-1} KOH electrolyte were also estimated and shown in Fig. 5b. It can be seen that the CV behaviors show a similar trend with those in acid electrolyte, indicating its good capacitive performance in alkaline electrolyte.

The galvanostatic charge–discharge curves measured at the current densities of 0.5, 1.0, 2.0, and 4.0 A g^{-1} for AC-3-600 in 1 mol L^{-1} H_2SO_4 and 6 mol L^{-1} KOH electrolytes, respectively, are shown in Fig. 6. It was observed that all the

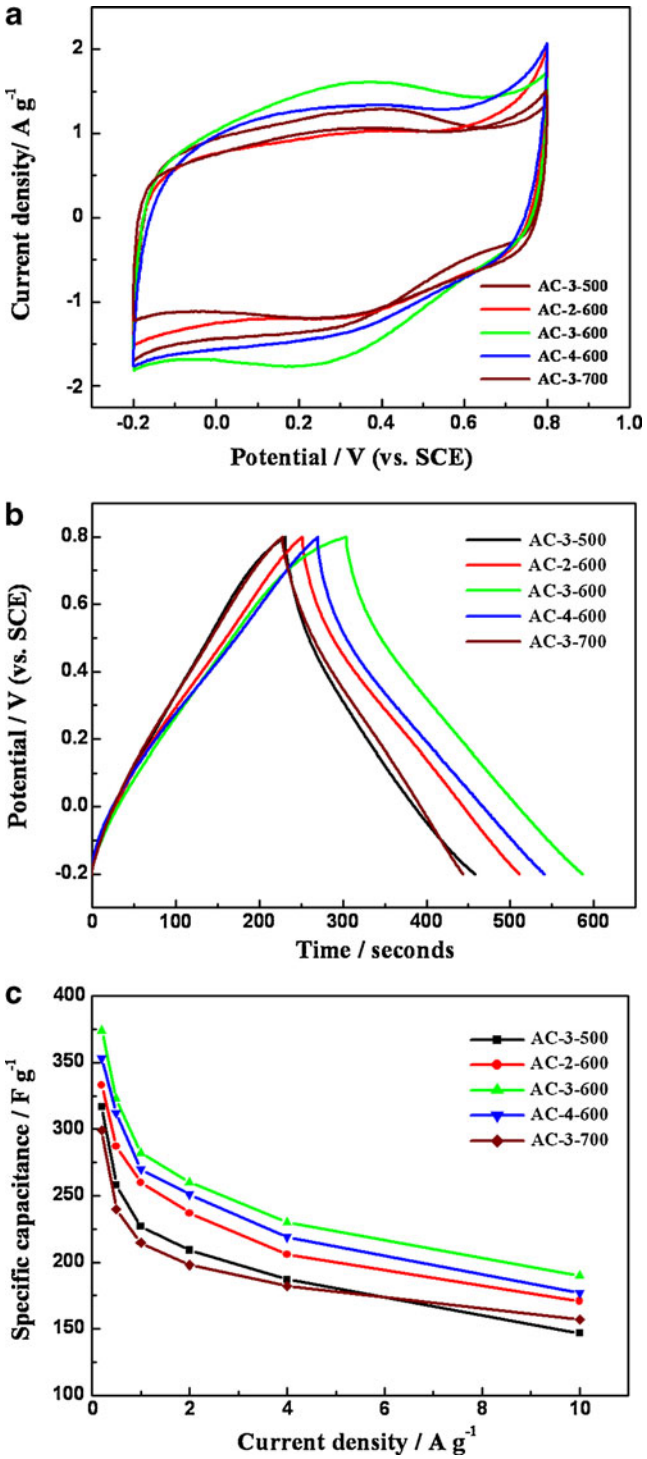

Fig. 4 The CVs at 5 mV s^{-1} (**a**) and the galvanostatic charge–discharge curves measured at 1 A g^{-1} for ACs (**b**) in 1 mol L^{-1} H_2SO_4 electrolyte and the influence of current density on specific capacitance of ACs derived from COS (**c**)

charge/discharge profiles of AC-3-600 at different current densities exhibit almost isosceles triangle curves, which reflect good charge/discharge capacitive performance. The specific capacitance of 323, 282, 260, and 230 F g^{-1} can be delivered from AC-3-600 in 1 mol L^{-1} H_2SO_4 electrolyte at the current density of 0.5, 1.0, 2.0, and 4.0 A g^{-1}, respectively. There has been a little reasonable decrease in the specific capacitance as expected when the electrolyte is changed to 6 mol L^{-1} KOH, which is due to the less pseudo-faradic capacitance contribution of oxygenated surface functionalities in KOH electrolyte [23]. The specific capacitance of 227, 212, 198, and 184 F g^{-1} can still be obtained in 6 mol L^{-1} KOH electrolyte at the current densities of 0.5, 1.0, 2.0, and 4.0 A g^{-1}, respectively, showing the acceptable specific capacitance in both acid and alkaline electrolytes.

For further understanding of the electrochemical performances, the cyclic charge–discharge tests were performed at a fair current density of 4 A g^{-1} in 1 mol L^{-1} H_2SO_4 and 6 mol L^{-1} KOH electrolytes, respectively, and the corresponding results are shown in Fig. 7. As shown in Fig. 7, the specific capacitance of AC-3-600 in 1 mol L^{-1} H_2SO_4 electrolyte is up to 230 F g^{-1} at the first cycle and keeps remarkably stable over 5,000 cycles. The specific

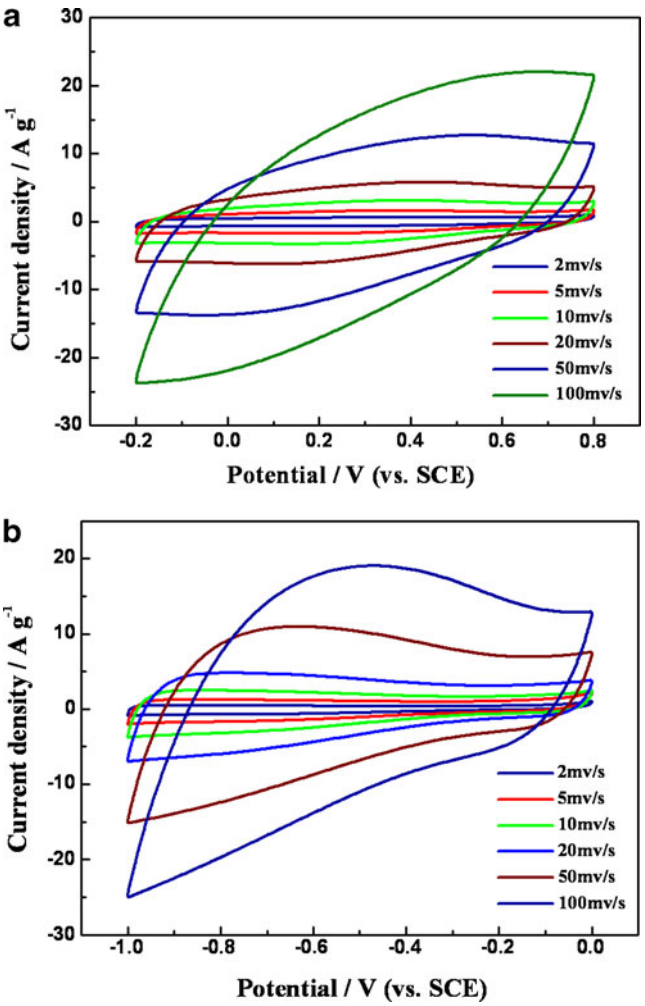

Fig. 5 Cyclic voltammograms at different scan rates for AC-3-600 in 1 mol L^{-1} H_2SO_4 (**a**) and 6 mol L^{-1} KOH (**b**) electrolytes, respectively

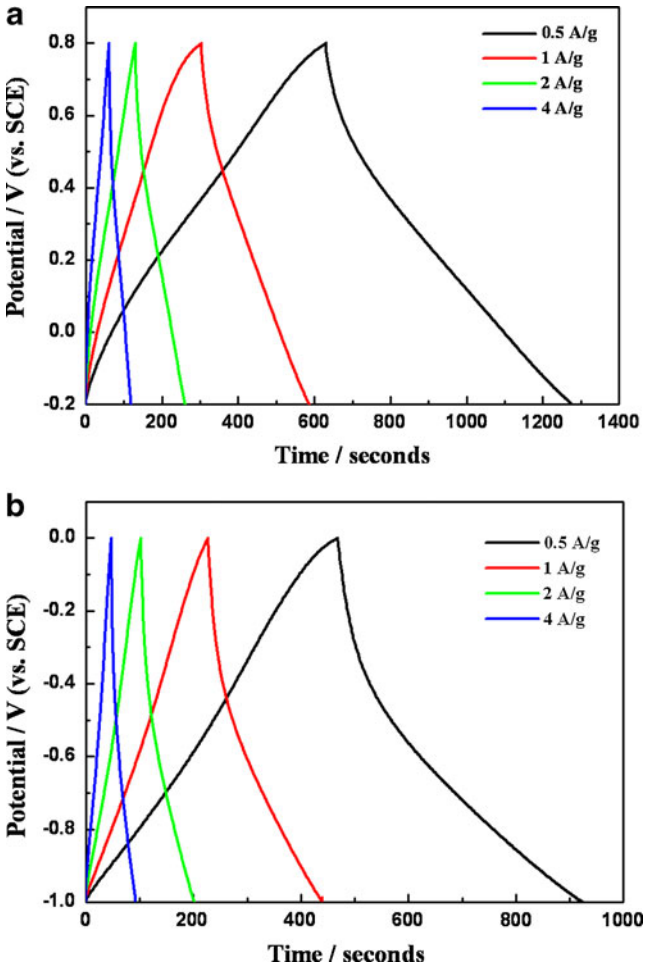

Fig. 6 The galvanostatic charge–discharge curves measured at different current densities for AC-3-600 in 1 mol L^{-1} H_2SO_4 (**a**) and 6 mol L^{-1} KOH (**b**) electrolytes, respectively

capacitance of AC-3-600 in 6 mol L^{-1} KOH electrolyte is 184 Fg^{-1} and 168 Fg^{-1} at the first and the 5,000th cycle, respectively, showing a high capacitance retention ratio of 91.3%. These results demonstrate that the activated carbons derived from COS exhibit good cycle stability and very high degree of reversibility during repetitive charge/discharge cycles in both acid and alkaline electrolytes. In addition, their corresponding coulomb efficiency can reach 100% (Fig. 8), which reveals that AC-3-600 electrode material has high utilization and stable coulombic efficiency in both acid and alkaline solutions.

Conclusions

A biomass raw material, *C. oleifera* shell, is used to prepare activated carbon electrodes by $ZnCl_2$ activation method. Carbonization temperature and $ZnCl_2$ impregnation ratio are two key factors that affect directly the pore development and subsequently the electrochemical performance of the

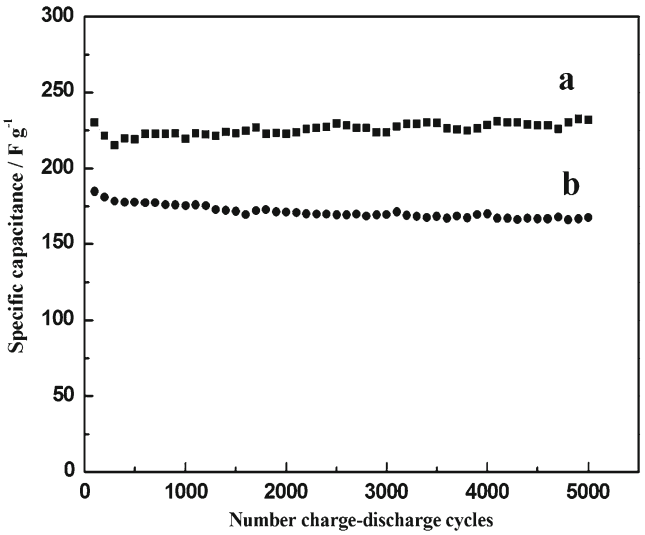

Fig. 7 Charge–discharge cycling stability of AC-3-600 at a current density of 4 A g^{-1} in 1 mol L^{-1} H_2SO_4 (**a**) and 6 mol L^{-1} KOH (**b**) electrolytes

resulting activated carbon. Activated carbon with a surface area of 1935 m^2 g^{-1}, total pore volume of 1.02 cm^3 g^{-1}, and especially the larger percentage of micropores (735 m^2 g^{-1}) has been produced at a final carbonization temperature of 600 °C and an impregnation ratio of 3 and exhibits excellent electrochemical properties in both acid and alkaline electrolytes. It shows the highest specific capacitances of 374 Fg^{-1} in 1 mol L^{-1} H_2SO_4 electrolyte at 0.2 A g^{-1} and also displays high-rate long-cycle electrochemical performance even at a current density of 4 A g^{-1}. The high specific capacitance of 266 Fg^{-1} at 0.2 A g^{-1} and excellent capacity retention of 91.3% at 4 A g^{-1} are also shown in the alkaline electrolyte

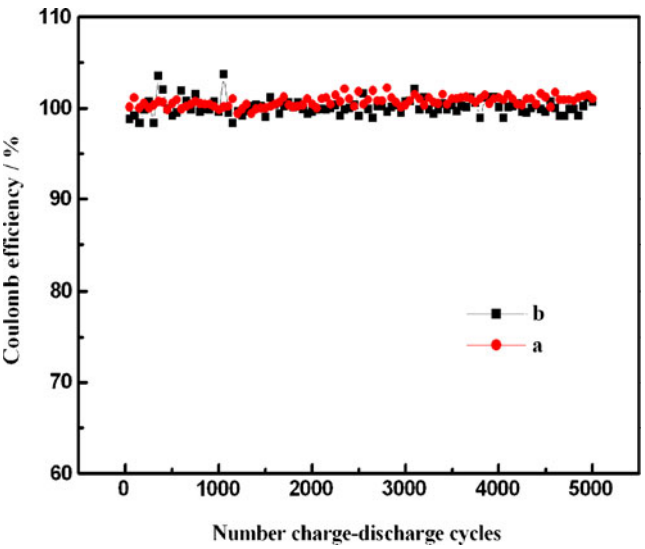

Fig. 8 Variation of coulombic efficiency of the AC-3-600 electrode with increasing cycle number at a current density of 4 A g^{-1} in 1 mol L^{-1} H_2SO_4 (**a**) and 6 mol L^{-1} KOH (**b**) electrolytes

for the AC. All these electrochemical results demonstrate the exciting possibility of preparing high-performance electrode material from biomass waste COS.

Acknowledgements This work was financially supported by the National Key Basic Research Program of China (973) (2007CB209703), National Natural Science Foundation of China (No. 206033040, No. 20873064), Key Lab.of Biomass Energy and Material, Jiangsu Province (2010 M001), and the Outstanding Young Scientists Incentive Foundation of Shandong Province (BS2010NJ007).

References

1. Xing W, Qiao SZ, Ding RG, Li F, Lu GQ, Yan ZF (2006) Carbon 44:216–224
2. Lota G, Centeno TA, Frackowiak E, Stoeckli F (2008) Electrochim Acta 53:2210–2216
3. Bentley P, Stone DA, Schofield N (2005) J Power Sources 147:288–294
4. Zhang LL, Zhao XS (2009) Chem Soc Rev 38:2520–2531
5. Gao B, Hao L, Fu QB, Su LH, Yuan CZ, Zhang XG (2010) Electrochim Acta 55:3681–3686
6. Hsieh CT, Chen WY, Lin JH (2009) Micropor Mesopor Mater 122:155–159
7. Scherdel C, Reichenauer G (2009) Micropor Mesopor Mater 126:133–142
8. Stoller MD, Park S, Zhu YW, An JH, Ruoff RS (2008) Nano Lett 8:3498–3502
9. Du X, Guo P, Song HH, Chen XH (2010) Electrochim Acta 55:4812–4819
10. Zhang LL, Zhou R, Zhao XS (2010) J Mater Chem 20:5983–5992
11. Subramanian V, Luo C, Stephan AM, Nahm KS, Thomas S, Wei BQ (2007) J Phys Chem C 111:7527–7531
12. Li X, Xing W, Zhuo SP, Zhou J, Li F, Qiao SZ, Lu GQ (2011) Bioresour Technol 102:1118–1123
13. Rufford TE, Hulicova-Jurcakova D, Fiset E, Zhu ZH, Lu GQ (2008) Electrochem Commun 10:1594–1597
14. Balathanigaimani MS, Shim WG, Lee MJ, Kim CH, Lee JW, Moon H (2008) Electrochem Commun 10:868–871
15. Wu FC, Tseng RL, Hu CC, Wang CC (2004) J Power Sources 138:351–359
16. Qiao WM, Yoon SH, Mochida I (2006) Energy Fuels 20:1680–1684
17. Kim YJ, Abe Y, Yanagiura Y, Park KC, Shimizu M, Iwazaki T (2007) Carbon 45:2116–2125
18. Bichat MP, Pinero R, Beguin F (2010) Carbon 48:4351–4361
19. Rufford TE, Hulicova-Jurcakova D, Khosla K, Zhu ZH, Lu GQ (2010) J Power Sources 195:912–918
20. Zhang QD, Peng WC, Liu QM, Tian H (2008) J Chin Cereals Oils Assoc 23:162–165
21. Xing W, Huang CC, Zhuo SP, Yuan X, Wang GQ, Hulicova-Jurcakova D, Yan ZF, Lu GQ (2009) Carbon 47:1715–1722
22. Nian YR, Teng H (2002) J Electrochem Soc 149:A1008–A1014
23. Andreas HA, Conway BE (2006) Electrochim Acta 51:6510–6520